Theoretical investigation of the vibronic phosphorescence spectra and quantum yields for iridium(III) complexes with 2-(2,5,2′,3′,4′,5′,6′-heptafluoro-biphenyl-4-yl)-pyridine as the primary ligand

Jiayi Guo, Xiao Pan, Junfeng Li *, Wenpeng Wu *, Jinglai Zhang *

Henan Provincial Engineering Research Center of Green Anticorrosion Technology for Magnesium Alloy, College of Chemistry and Chemical Engineering, Henan University, Kaifeng 475004, People's Republic of China

ARTICLE INFO

ABSTRACT

Cyclometalated Ir(III) complexes are widely used as phosphorescent materials in organic light-emitting diodes. In this work, the vibrationally resolved phosphorescence spectra of an experimental reported and four novel designed Ir(III) complexes with 2-(2,5,2′,3′,4′,5′,6′-heptafluoro-biphenyl-4-yl)-pyridine (HFYP) as primary ligand are investigated by theoretical calculations. The ancillary ligands are 3-(pentafluorophenyl)-pyridin-2-yl-1,2,4-triazolate (**exp3**), 3-(trifluoromethyl)-pyridin-2-yl-1,2,4-triazolate (**5**), 5-methylsulfonyl-2-oxyphenyl-2-oxazole (**6**), 5-trifluoromethyl-2-oxyphenyl-2-oxazole (**7**), 2-(3-(trifluoromethyl)-1H-1,2-diazol-5-yl)pyridine (**8**), respectively. Phosphorescence spectra show that there are mainly two strong peaks, which can be ascribed as low-frequency vibrational modes such as the rotation of ligand plane, and benzene ring/pyridine ring in ligand HFYP1 skeleton vibration coupled with C—H in pyridine ring in plane bending vibration. The phosphorescence quantum yields were quantitatively determined by evaluating radiative decay rate constant k_r, intersystem crossing rate constant k_{ISC} and temperature-dependent nonradiative decay rate constant $k_{nr}(T)$. It shows that the quantum yields of compounds **exp3**, **5** and **8** are relative higher, while those of compounds **6** and **7** are much smaller. This is mainly caused by larger $k_{nr}(T)$ of compounds **6** and **7**. It is anticipated that in Ir(III) complex with HFYP primary ligand, pyridin-2-yl-1,2,4-triazolate, 1,2-diazol-5-yl-pyridine are good ancillary ligand, while 2′-oxyphenyl-2-oxazoline is not appropriate to be ancillary ligand.

© 2019 Published by Elsevier B.V.

1. Introduction

For the next-generation illumination sources and flat-panel display [1–4], phosphorescent iridium(III) complexes have gained intense research interest [5–8] because of their wide applications in organic light-emitting diodes (OLEDs). They show high phosphorescence quantum efficiencies, short phosphorescent lifetimes and good color tunability [9,10] by modifying their structure. Among them, white OLED (WOLED) can result from simultaneous emission of two (most commonly blue and orange) or three (red, green and blue) emitting components blended in a single host material or confined in different stacked layers.

Recently, Ragni et al. synthesized a new heteroleptic iridium complex, namely iridium(III) bis[2-(2,5,2′,3′,4′,5′,6′-heptafluoro-biphenyl-4-yl)-pyridinato-N,C2'][3-(pentafluorophenyl)-pyridin-2-yl-1,2,4-triazolate] (Ir-F19), bearing highly fluorinated cyclometalating ligands and acting as an efficient blue-green phosphor [11]. Thus, a two-color based stacked WOLED was obtained, with CRI of 76 and 10.5 cd/A luminous efficiency at 100 cd/m², almost constant (10.1 cd/A) up to 1000 cd/m², using Ir-F19 and the commercial orange emitter bis(2-methyldibenzo[*f,h*]quinoxaline)(acet-ylacetonate)iridium [Ir(MDQ)₂(acac)] in a two stacked layer device architecture. Fluorination can increase volatility favouring vapour deposition, enhance electron mobility, and prevent close packing that can cause electroluminescence self-quenching of molecular active materials in devices [12–14]. It is also reported that the bulky pentafluorophenyl markedly reduce concentration quenching of phosphorescence by the steric hindrance effect [15]. Therefore, 2-(2,5,2′,3′,4′,5′,6′-heptafluoro-biphenyl-4-yl)-pyridine (HFYP) is likely to be a suitable primary ligand for potential efficient phosphors. So we want to investigate the effect of ancillary ligand on the phosphorescence spectra and quantum yield in Ir(III) complex with HFYP as primary ligand.

As is known to all, experimental discovery is limited by high costs and time-consuming process of synthesis. On the contrary, theoretical

* Corresponding authors.
E-mail addresses: junfenl@kth.se (J. Li), wuwp@henu.edu.cn (W. Wu), zhangjinglai@henu.edu.cn (J. Zhang).

calculation might be a reliable and important tool to illustrate properties of the well-known chemical species and to predict the novel one [16–19]. The shortage of efficient method to evaluate the photoluminescence quantum yield (PLQY) is one of the key challenges in the field of theoretical research due to complicated nonradiative decay process. In the past several years, significant progresses have been made to determine the PLQY theoretically, especially the nonradiative decay rate constant. Che's group calculated nonradiative decay rate constant with the convolution method in which the low-frequency modes are treated in the strong coupling limit and the high-frequency modes in the weak coupling limit [20]. Escudero proposed a simplified expression to compute relative PLQY with radiative transition rate constant and the activation energy for the limiting step related with temperature-dependent nonradiative decay channel [21]. Zhang's group has also carried out a series of work on the calculation of PLQY for transition-metal complexes with qualitative, semi-quantitative, and quantitative methods [22–29]. Recently, Shuai's group presented a general approach for computing the photoluminescence efficiencies of Ir(III) complexes by considering all possible competing excited-state deactivation processes and explicitly including the strongly temperature-dependent ones [30,31]. It is shown to be an efficient and reliable approach for the calculation of PLQY of Ir(III) complexes. This provides us a simple method to calculate the PLQY quantitatively, which is one aim of this work.

From another point of view, photo emission is intrinsically involved in the effect of the nuclear motions of molecules. Vibronic spectra are essential to straightforwardly compare with experimental data and find the mode-specific effect on the spectra [29,32]. These fine spectra can then be used to calculate the Commission Internationale de l'Eclairage (CIE) coordinates. Thus another aim in this study is to simulate the phosphorescent spectra with fine structures including vibronic transitions.

In this work, five Ir(III) compounds with HFYP as primary ligand are selected, including Ir-F19 (**exp3**) which was synthesized in Ref [11] and four theoretically designed compounds (see Fig. 1). Therein, the ancillary ligands are based on previous literatures [3,33,34].

The paper is organized as follows. In Section 2, we briefly present a general description of the computational methods used in this paper. Section 3 shows the results and discussions including geometries, vibrationally resolved phosphorescence spectrum, quantum yield. Finally, conclusions are given in Section 4.

2. Computational details

The ground-state and triplet excited-state geometries for all investigated Ir(III) complexes were optimized by Becke's three-parameter hybrid exchange functional combined with the Lee-Yang-Parr correlation functional (B3LYP) [35,36], in combination with the LANL2DZ pseudopotential [37,38] for the Ir atom and 6-31G(d) atomic basis set [39] for other atoms. According to previous studies [22–24,26], the temperature-dependent nonradiative decay rate constant was quatitatively evaluated via constructing the potential energy surfaces of the kinetic scheme $^3MLCT \overset{^3TS}{\to} {}^3MC \overset{MECP}{\to} S_0$, where ^3MLCT refers to metal-to-ligand charge transfer state, ^3MC is metal centered state, S_0 is the ground singlet state, ^3TS is the transition state between ^3MLCT and ^3MC states, and MECP is the minimum energy crossing point connecting ^3MC and S_0 potential energy surface. Therein, the ^3MC state, ^3TS and MECP were located by the UB3LYP method. The geometry of MECP was optimized using Gaussian 09 together with the code developed by Lu, which is a modified version of Harvey's MECP program [40,41]. On the basis of the lowest optimized triplet states, the vertical emission energies were simulated by the ΔSCF-DFT (Delta-self-consistent field density-functional theory) calculations [42,43]. Based on the ground-state geometries, the spin-orbit coupling matrix elements and transition dipole moments between singlet and triplet states were respectively evaluated using the linear and quadratic response theories in the framework of TDDFT with the B3LYP functional, as implemented in the Dalton program [44]. During the calculations, the solvent effect was considered by the polarized continuum model (PCM) with acetonitrile as solvent [45]. Except for the special mentioned, all calculations were performed by the Gaussian 09 program [46]. The radiative rate constant (k_r),
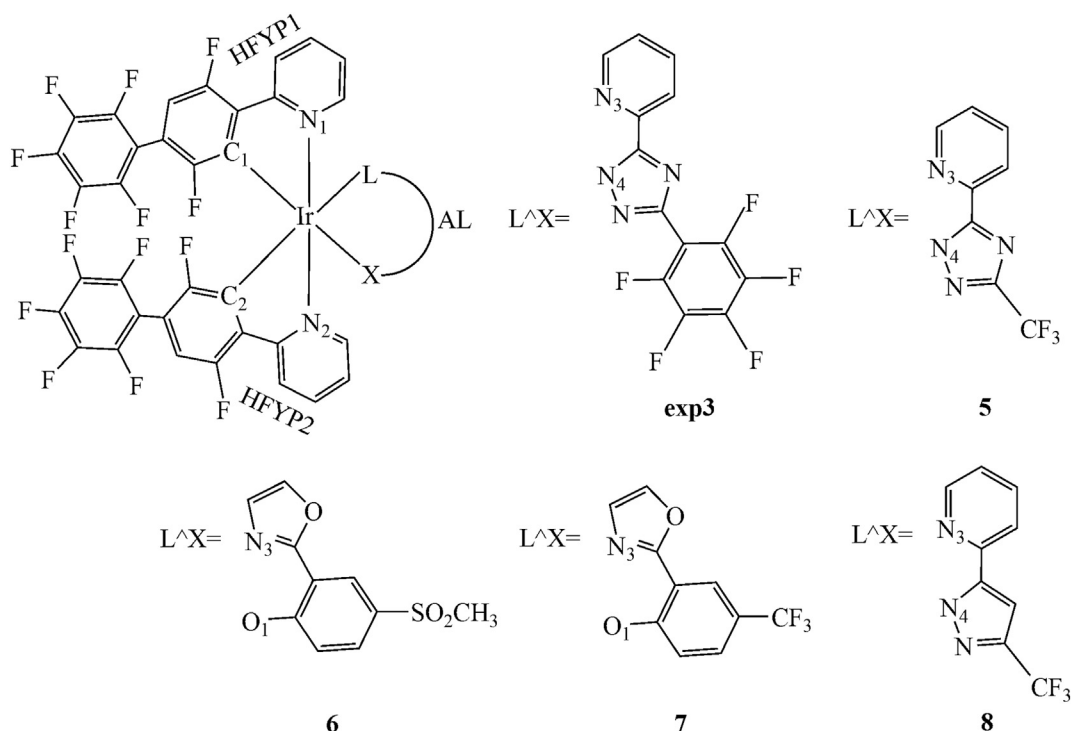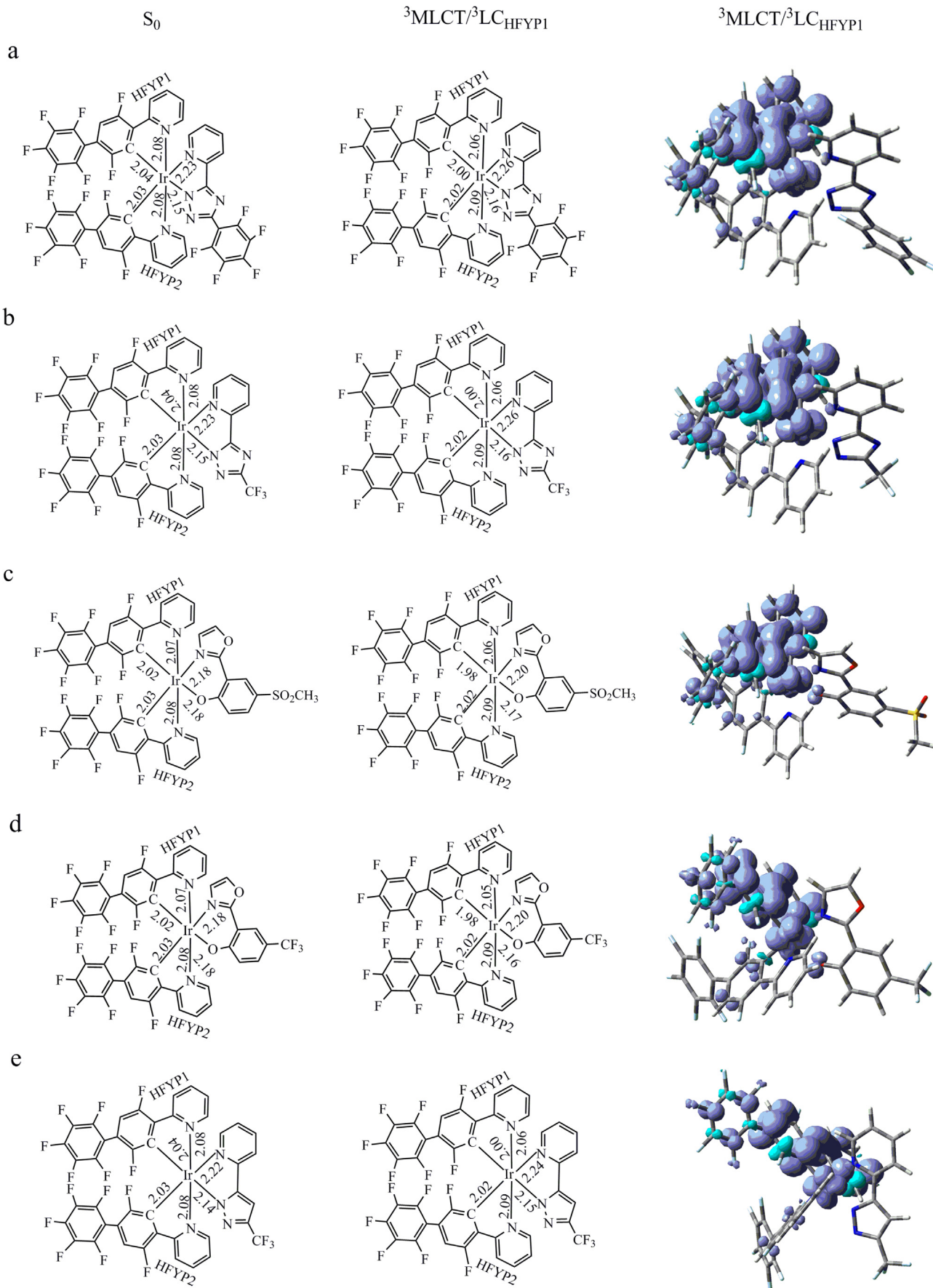

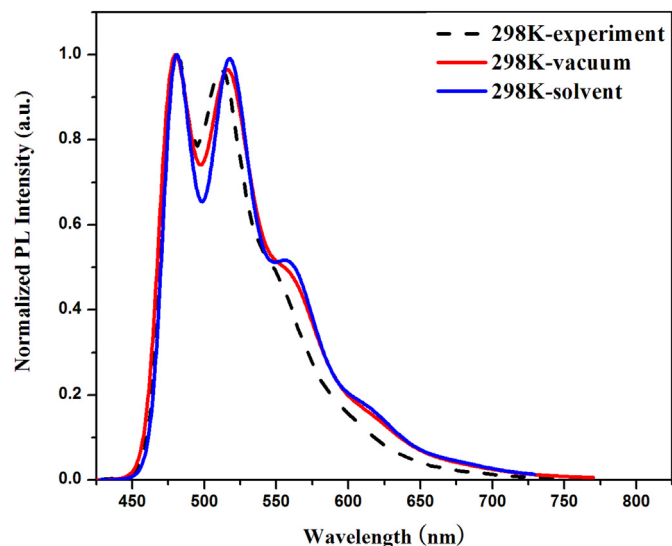**Fig. 1.** Sketch structures of all the investigated Ir(III) complexes.

Fig. 2. Selected bond lengths (Å) in the optimized structures of S$_0$, the lowest triplet excited states of complexes **exp3** (a), **5** (b), **6** (c), **7** (d), and **8** (e) in acetonitrile solvent. The computed spin density distributions at the B3LYP/6-31G(d)-LANL2DZ level are also presented. Purple color represents the positive value that means α-electrons are more than β-electrons, and green color represents negative value.

Table 1
Computed vertical phosphorescent emission energy (E_v) and 0–0 transition energies (E_{0-0}) in acetonitrile.

Emission energy	exp3[a]	5	6	7	8
E_v [eV/nm]	2.33/533	2.33/532	2.29/541	2.28/544	2.32/533
E_{0-0} [eV/nm]	2.53/490	2.53/490	2.48/500	2.47/502	2.53/491

[a] The experimental emission peaks are 480 nm (2.58 eV) and 512 nm (2.42 eV) [11].

Table 2
The values of the electronic transition dipole moment (μ) (Debye) between S_0 and T_1 states of complexes exp3, 5, 6, 7 and 8 in acetonitrile solvent and vacuum.

μ (Debye)	exp3	5	6	7	8
acetonitrile	0.21	0.20	0.24	0.25	0.21
vacuum	0.22	0.21	0.24	0.26	0.22

Table 3
Computed k_r, k_{ISC}, and k_{nr} (T), Φ_P values from the triplet excited states of complexes exp3, 5, 6, 7 and 8 in acetonitrile solvent.

Items	exp3	5	6	7	8
k_r (s^{-1})	7.84×10^4	7.13×10^4	9.79×10^4	1.02×10^5	8.22×10^4
k_{ISC} (s^{-1})	1.98×10^5	1.79×10^5	3.84×10^4	1.07×10^5	2.03×10^5
k_{nr} (T) (s^{-1})	3.14×10^4	4.31×10^4	2.03×10^6	3.26×10^6	2.22×10^4
Φ_P	0.25	0.24	0.05	0.03	0.27

Fig. 3. The comparison of the calculated and experimental spectra of exp3 at 298 K (The calculated spectrum was shifted 29 nm and 22 nm to blue in vacuum and acetonitrile solvent respectively).

nonradiative intersystem crossing rate constant (k_{ISC}) rate and vibrationally-resolved emission spectrum calculations were performed with the MOMAP suite of programs [47–50]. In the simulation of vibrationally-resolved emission spectrum, a scale factor of 0.96 is used to calibrate the vibrational frequencies.

3. Results and discussion

3.1. Ground-state and the triplet excited-state geometries

The selected optimized geometric parameters of the singlet ground state (S_0) of five Ir(III) complexes in acetonitrile solvent are shown in Fig. 2. The ball-and-stick models of fully optimized ground state geometrical structures are presented in Fig. S1. All the investigated Ir(III) complexes present a slight distorted octahedral symmetry coordinated with C1, N1, C2, N2 atoms in two principal ligands (HFYP) and N3, N4/
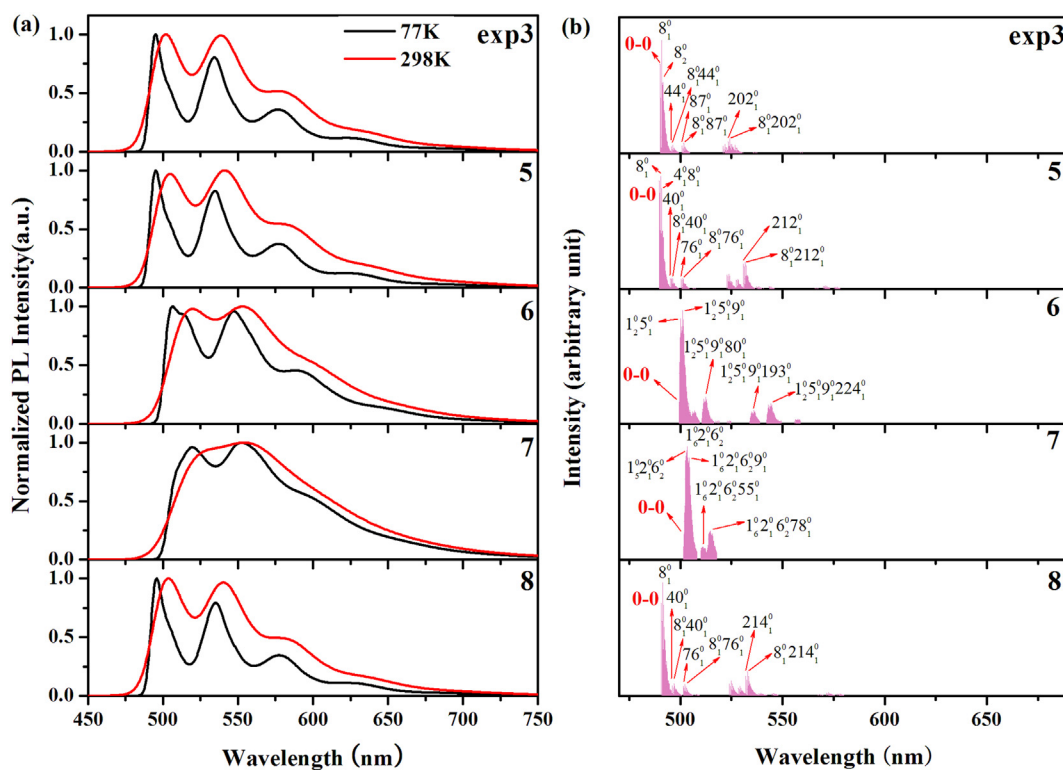
Fig. 4. In acetonitrile solvent, the calculated emission spectra (a) at finite temperatures and (b) at 0 K for compounds exp3, 5, 6, 7 and 8. (The individual vertical spectral lines can be assigned to the involved vibrational states of the S_0 state. Vibrational contributions are shown with pink vertical lines labeled by n_x^y, where n is the normal mode number, x indicates the quanta in the ground state deposited on normal mode n, while y is the quanta in the excited state deposited on normal mode n.)

Table 4

The values of adiabatic excitation energy (ΔE_{ad}) (eV), total reorganization energy $\lambda = \sum\limits_{k} \lambda_k$ (eV) and the SOC matrix elements (cm^{-1}) between S_0 and T_1 states of complexes **exp3**, **5**, **6**, **7** and **8** in acetonitrile solvent.

Items	exp3	5	6	7	8
ΔE_{ad} (eV)	2.64	2.63	2.58	2.57	2.63
$<T_1|\hat{H}_{SO}|S_0>$ (cm^{-1})	174.12	174.92	187.42	193.43	179.25
λ (eV)	0.32	0.32	0.32	0.36	0.31

O1 atoms in one ancillary ligand. The accurate triplet state geometries and emission spectra are important to study the phosphorescent properties. The optimized geometries of the lowest triplet excited states for the five compounds are plotted in Fig. 2 along with the key bond lengths, respectively. It is a ^{3}MLCT/^{3}LC (ligand-centered) state. The corresponding values in vacuum are listed in Fig. S2.

For the lowest triplet states of the five compounds, the spin density is distributed over the HFYP1 ligand and Ir atom, which is in accordance with the contracted Ir—N1 and Ir—C1 bonds. It is worth noting that the bond length of Ir—N1/N2 is longer than that of Ir—C1/C2 in the HFYP
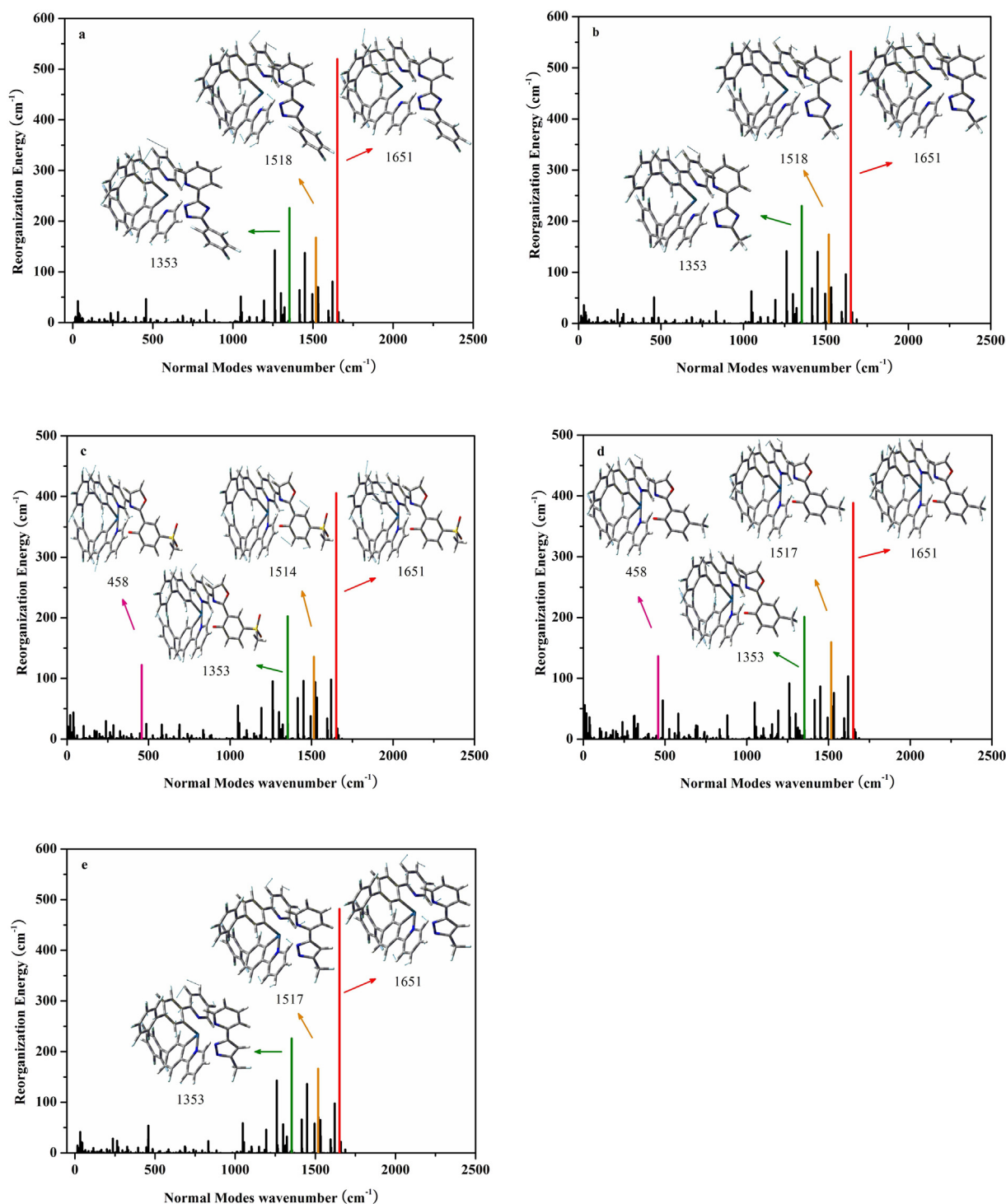
Fig. 5. Calculated reorganization energy of each normal mode for **exp3** (a), **5** (b), **6** (c), **7** (d), and **8** (e) in acetonitrile solvent. The displacement vectors of its most relevant modes are depicted.

a

b
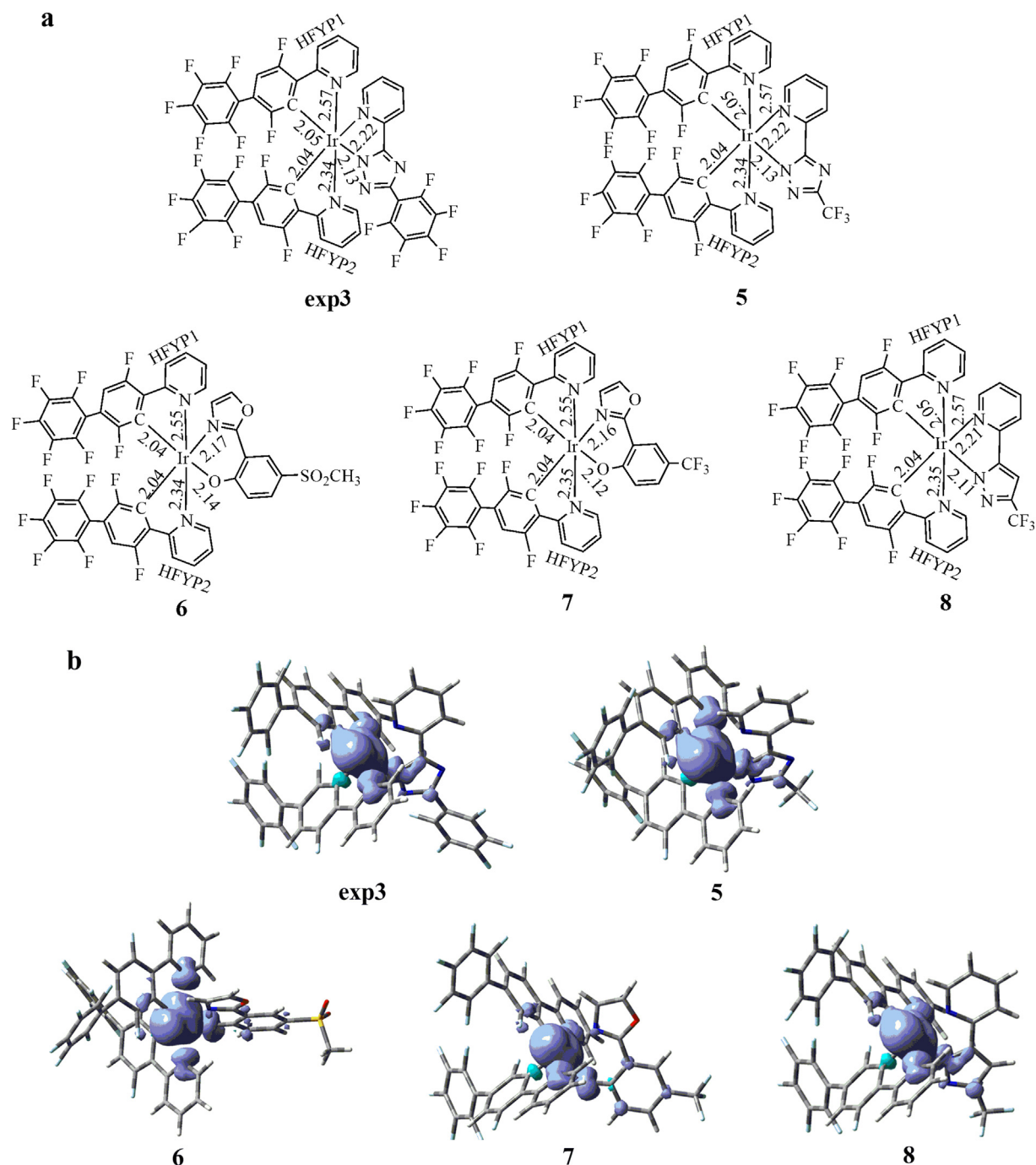
Fig. 6. (a) Selected bond lengths (Å) in the optimized structures of ^{3}MC states for Ir(III) complexes **exp3**, **5**, **6**, **7**, and **8** in acetonitrile. (b) The computed spin density distributions at the B3LYP/6-31G(d)-LANL2DZ level, purple color represents the positive value that means α-electrons are more than β-electrons, and green color represents negative value.

ligand of the S_0 and ^{3}MLCT/LC states, while in the ancillary ligand the bond length of Ir—N3 is longer than that of Ir—N4, both of which are longer than that of Ir—N1/N2. For compounds **6** and **7**, the bond length of Ir—N3 is obviously shorter than that of the other compounds both in S_0 and ^{3}MLCT/LC states.

3.2. Phosphorescence spectra

The vertical phosphorescence emission energy and 0–0 transition energy are listed in Table 1, as well as the available experimental values [11]. From Table 1, it can be found that the 0–0 transition energy of compound **exp3** is closer to the experimental maximum, in accordance with previous studies [24,26,27]. It can also be seen from Table 1 that the

emission energies of compounds **5** and **8** are similar to **exp3**, while those of compounds **6** and **7** decrease about 0.05 eV, which will lead to red shift in the phosphorescent spectra.

The vibrationally resolved emission spectra are very helpful to get deep insight into the photophysical properties. The simulated spectrum of compound **exp3** shows good agreement with the experimental one (see Fig. 3). Fig. 4 shows the calculated spectra at 298, 77 and 0 K for all the compounds. At low temperatures, the vibrationally resolved spectra can be used to clarify the electronic transition properties and electron-phonon interaction [30]. For every compound, the spectrum exhibits fine structures at low temperatures. The origin of the emission bands and the contribution of the vibration modes to such bands for all compounds can be fairly figured out from the spectra at 0 K as shown in

Fig. 4. The corresponding vibrational modes in vacuum and acetonitrile solvent are plotted in Fig. S3.

For compound **exp3**, it can be seen that the spectral features in the experiment were well reproduced in the simulated spectrum, including two strong emission peaks. The emission peak at 502 nm (480 nm in the experiment) is mainly contributed by some low-frequency vibrational modes such as the rotation of ligand plane, partly contributed by 0–0 transition. The emission peak at 539 nm (512 nm in the experiment) is mainly caused by the HFYP1 ligand whose benzene ring and pyridine ring skeleton vibration transitions coupled with C—H of pyridine ring in plane bending vibration transitions. Compared with the most intense emission peak (around 0–0 transition), the intensities of the other peaks increase with the temperature rising. Moreover, the emission spectra red shifts with increasing temperatures. Besides, the nature of the vibrational satellites is related to the distributions of the Huang-Rhys factors (see Fig. S4), which are the key parameters to characterize vibronic couplings. According to the simulated emission spectrum (unshifted) under 298 K, the CIE1931 coordinates are calculated as (0.34, 0.58), which are comparable with (0.26, 0.51) obtained by the experimental spectrum [11]. The CIE1931 coordinates of the other molecules are calculated as (0.35, 0.58), (0.39, 0.58), (0.41, 0.56), (0.34, 0.59), respectively. The chromaticity diagram is presented in Fig. S5. It can be seen that CIE coordinates of compounds **exp3**, **5** and **8** are similar, while x coordinates of compounds **6** and **7** are a little bigger.

Compared with the calculated spectra in vacuum (see Fig. S6), the maximum emission peaks in acetonitrile solvent shift to blue within 10 nm; the spectral characteristics remains and the spectral shape is almost unchanged.

3.3. Phosphorescence quantum efficiency

The photoluminescence quantum yield is one of the most vital factors to assess the performance of phosphors. The quantum yield is determined by the following relationship [31]:

$$\Phi_P(T) = \frac{k_r}{k_r + k_{ISC} + k_{nr}(T)} \quad (1)$$

where k_r is the radiative decay rate and k_{ISC} is the nonradiative intersystem crossing rate (ISC), which in principle is temperature-dependent through vibration population, and $k_{nr}(T)$ is the strongly temperature-dependent nonradiative decay rate associated with the population of the ^3MC well.

3.3.1. Radiative rate constant (k_r)

The radiative decay rate constant was calculated by integrating over the whole emission spectrum [30]:

$$k_r(T) = \int \sigma_{em}(\omega, T) d\omega \quad (2)$$

$$\sigma_{em}(\omega, T) = \frac{4\omega^3}{3\hbar c^3} \sum_{u,v} P_{iv}(T) \left| \left\langle \Theta_{fu} \left| \vec{\mu}_{fi} \right| \Theta_{iv} \right\rangle \right|^2 \delta(\omega_{iv,fu} - \omega) \quad (3)$$

Here P_{iv} is the Boltzmann distribution function of the initial state at certain temperature; Θ is the nuclear vibrational wave function. $\vec{\mu}_{fi} = \langle \Phi_f | \vec{\mu} | \Phi_i \rangle$ is the electric transition dipole moment between two electronic states. ω, c, $\hbar$, T represent frequency, speed of light, reduced Planck's constant and thermodynamic temperature, respectively.

In the formalism for spectrum calculation, the electric transition dipole moment (μ), adiabatic excitation energy (ΔE_{ad}) and vibronic coupling are three fundamental physical parameters [44,51]. As pointed out by previous work, the vibronic couplings mainly determine the shape and width of an emission spectrum but hardly change the integration of the spectrum [21]. Therefore, the radiative rates are primarily controlled by μ and ΔE_{ad} between S_0 and T_1 states. From the Eq. (3), it

can be seen that the larger μ (see Table 2) would be favorable for the improvement of k_r, and Table 3 lists the radiative rate constants in acetonitrile solvent for all the compounds. Compounds **6** and **7** with the bigger k_r are in accordance with their larger μ. Comparison of μ in acetonitrile and vacuum, no significant change is found. Calculated k_r, k_{ISC}, and k_{nr} (T), Φ_P values from the triplet excited states of complexes **exp3**, **5**, **6**, **7** and **8** in vacuum are listed in Table S2 of supplementary material.

3.3.2. Nonradiative intersystem crossing rate constant (k_{ISC})

For Ir(III) complexes with large SOCs, first-order perturbation theory is a good approximation to compute the nonradiative intersystem crossing (k_{ISC}) rate [30]. The values of adiabatic excitation energy (ΔE_{ad}), total reorganization energy and the SOC matrix elements between S_0 and T_1 states of complexes **exp3**, **5**, **6**, **7** and **8** in vacuum are listed in Table S3 in supplementary material. By applying the short-time approximation the first-order perturbation theory formula is simplified under the framework of the displaced harmonic oscillator model to intuitively analyze the nonradiative intersystem crossing rate constant (k_{ISC}) [30].

$$\ln[k_{ISC}(T_1 \to S_0)] = -\frac{\left(\Delta E_{ad} - \sum_k \lambda_k\right)^2}{4 \sum_k \lambda_k \overline{E}_k}$$
$$+ \ln\left(\frac{1}{\hbar} \left| \left\langle S_0 \left| \hat{H}_{SO} \right| T_1 \right\rangle \right|^2 \sqrt{\frac{\pi}{\sum_k \lambda_k \overline{E}_k}}\right) \quad (4)$$

where ΔE_{ad} denotes the adiabatic excitation energy; λ_k is the reorganization energy for the kth mode; $\overline{E}_k = (\overline{n}_k + 1/2)\hbar\omega_k$ is the average vibration energy and $\overline{n}_k$ is the phonon occupation number; $\hbar$, ω_k, k_B, T represent reduced Planck's constant, frequency, the Boltzmann constant and thermodynamic temperature, respectively. From Eq. (4), it can be seen that adiabatic excitation energy, spin-orbit coupling and reorganization energy between T_1 and S_0 are three key factors to govern the nonradiative intersystem crossing rate constant. The ΔE_{ad} and SOC in acetonitrile are listed in Table 4.

From Tables 3 and 4, we can see that the k_{ISC} of compounds **6** and **7** are significantly smaller than the other three molecules even if they have larger SOC values. This is mainly caused by the other two factors. The reorganization energy of each normal mode for the five compounds are displayed in Fig. 5. The distributions of λ_k for these compounds are similar. The normal modes in the 1000–1700 cm^{-1} region predominantly contribute to the k_{ISC} value of all compounds (see the
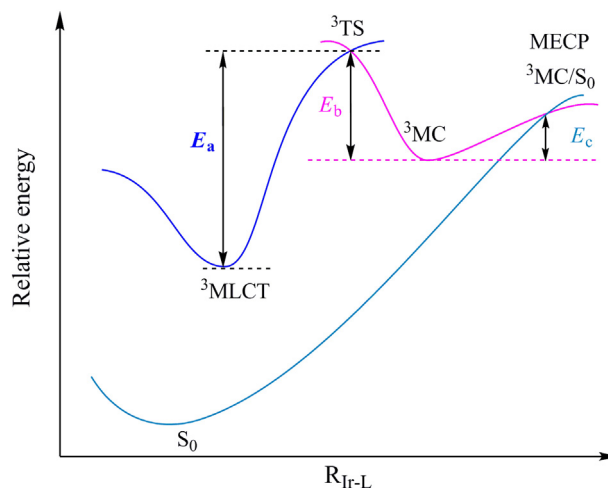

Fig. 7. Schematic potential energy profiles of the deactivation pathway via the ^3MC state for all complexes.
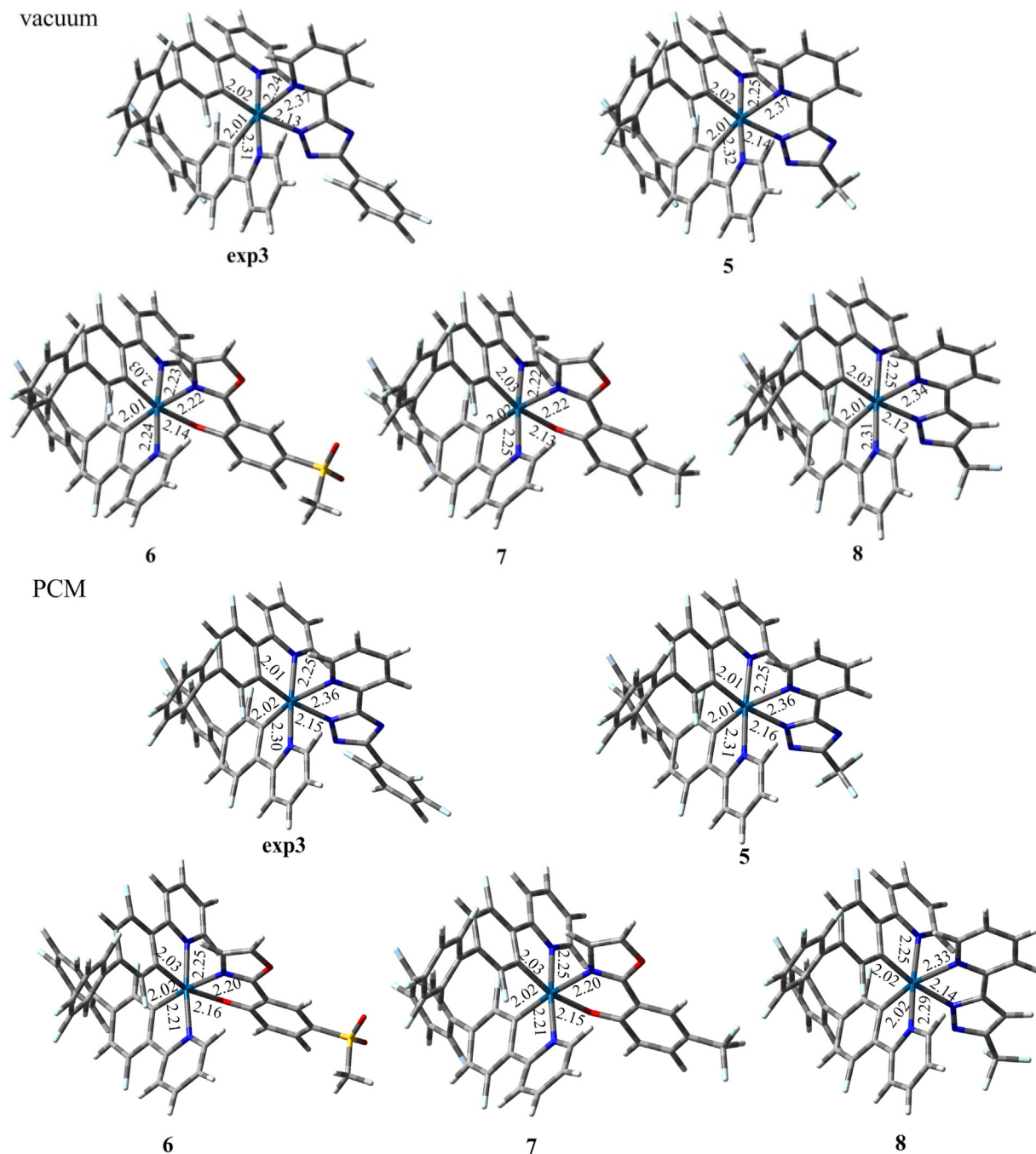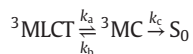
Fig. 8. The structures of transition state for Ir(III) complexes **exp3**, **5**, **6**, **7**, and **8** at the B3LYP/6-31G(d)-LANL2DZ level of theory in vacuum and acetonitrile.

displacement vectors of its three most relevant modes in Fig. 5, and it involves benzene ring and pyridine ring in HFYP1 ligand skeleton vibration transitions coupled with C—H of pyridine ring in plane vibration transitions). It should be noted that in the high frequency region, λ_k of the normal mode at 1651 cm^{-1} in compounds **exp3**, **5** and **8** is about 500 cm^{-1}, while that in compounds **6** and **7** is only about 400 cm^{-1}; the normal mode at 458 cm^{-1} in compounds **6** and **7** (benzene ring and pyridine ring deformation vibration in the primary ligands) contribute to the reorganization energies more than 100 cm^{-1}, while that in compounds **exp3**, **5** and **8** is less than 50 cm^{-1}.

3.3.3. Temperature-dependent nonradiative rate constant (k_{nr} (T))

The temperature-dependent nonradiative decay pathway is characterized by population of the ^{3}MC well through a transition state (TS) and the irreversible recovery of the ground-state (S$_0$) geometry through the

S$_0$/^{3}MC minimum energy crossing point (MECP). Therein, the spin density of ^{3}MC state is mainly populated in Ir atom (see Fig. 6). To get an insight into the temperature-dependent nonradiative decay process, the potential energy curves of the deactivation pathway from the ^{3}MLCT/^{3}LC to S$_0$ state via the ^{3}MC state are constructed, which are plotted in Fig. 7. Thus,

$$^3\text{MLCT} \underset{k_b}{\overset{k_a}{\rightleftharpoons}} {}^3\text{MC} \xrightarrow{k_c} \text{S}_0$$

Using the steady-state approximation and assuming this complex kinetic scenario, the k_{nr} (T) decay rate has the following form [31].

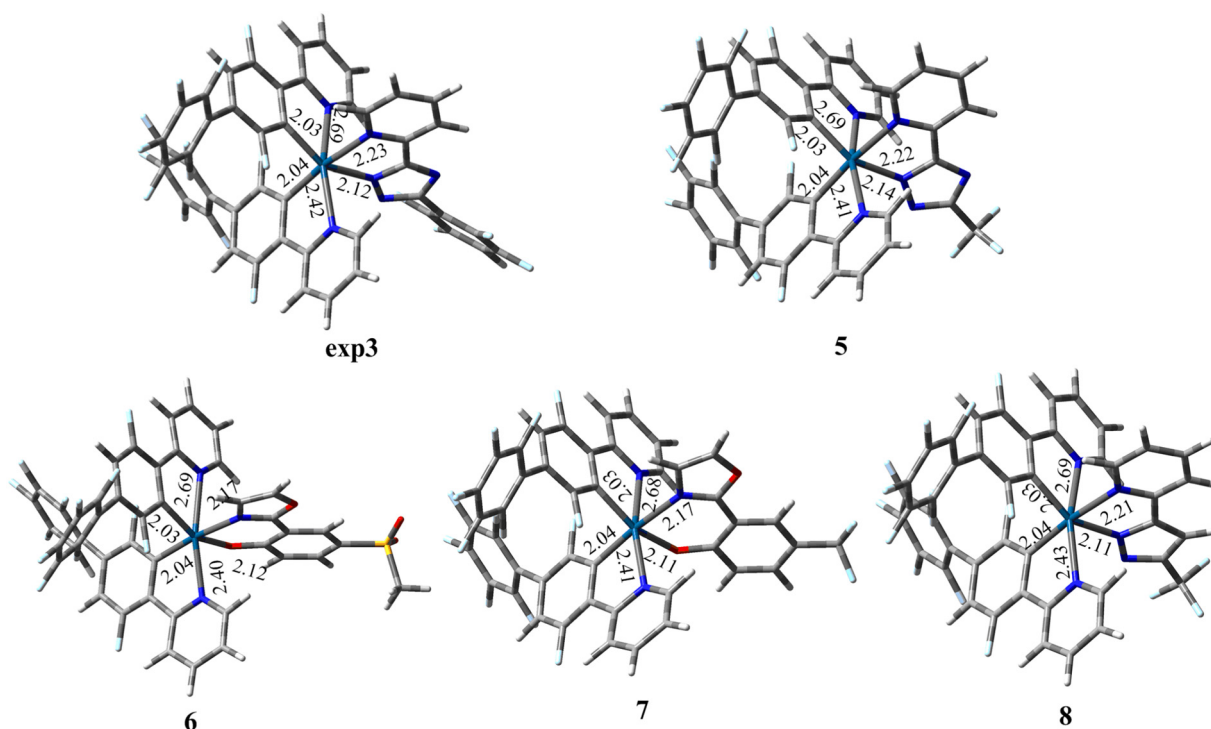$$k_{nr}(T) = k_c k_a / (k_c + k_b) \tag{5}$$

Fig. 9. The structures of MECP for Ir(III) complexes **exp3**, **5**, **6**, **7**, and **8** at the B3LYP/6-31G(d)-LANL2DZ level of theory in vacuum.

where k_a, k_b, and k_c (i.e., k_n) can be expressed as

$$k_n = A_n \exp(-E_n/k_B T) \qquad (6)$$

E_n is the activation energy, which is shown in Fig. 7; A_n is its corresponding pre-exponential factor; and k_B is the Boltzmann constant.

Under these circumstances, Eq. (5) can straightforwardly be approximated as

$$k_{nr}(T) = A_0 A \exp(-E_a/k_B T) \qquad (7)$$

where A_0 stands for a temperature-dependent Boltzmann prefactor in accordance to Eq. (5), i.e.,

$$A_0 = \frac{1}{1 + \exp\left(\frac{E_c - E_b}{k_B T}\right)} \qquad (8)$$

and herein the pre-exponential factor for the ^{3}MLCT → ^{3}MC transformation of A is set as 1.70×10^{13} s^{-1} according to previous study [31]. Activation barriers of the temperature-dependent nonradiative pathway and A_0, a temperature-dependent Boltzmann prefactor for all complexes in vacuum are listed in Table S4 in supplementary material.

The relevant structures of TS are displayed in Fig. 8. The corresponding bond lengths in vacuum and in acetonitrile are similar. Furthermore, the corresponding bond lengths of different compounds are also similar, except of much shorter Ir—N3 bonds in compounds **6** and **7**. For

Table 5
Activation barriers of the temperature-dependent nonradiative pathway and A_0, a temperature-dependent Boltzmann prefactor for all complexes in acetonitrile solvent.

Items	exp3	5	6	7	8
E_a (kcal/mol)	11.91	11.72	9.44	9.16	12.12
E_b (kcal/mol)	7.27	6.69	5.41	5.33	7.67
E_c (kcal/mol)	2.23	2.24	2.49	2.23	2.55
A_0	0.9998	0.9995	0.9928	0.9947	0.9998

example, Ir—N3 in compound **6** is 0.16 Å shorter than that in compound **exp3**. This may result in relative stable TS state in compounds **6** and **7**.

The relevant structures of MECP are shown in Fig. 9. The bond length of Ir—N3 in compounds **6** and **7** is a little shorter than that in the other compounds.

For all the compounds, the value of E_b is larger than E_c, which are both smaller than E_a. So the barrier to populate the TS (E_a) is the rate-limiting step of this decay pathway. The specific values of E_a, E_b, E_c, A_0 are listed in Table 5. From Eq. (4), the $k_{nr}(T)$ decay rates of compounds **6** and **7** are much larger due to their smaller E_a.

According to the calculation results in Table 3, even if compounds **6** and **7** have larger k_r and smaller k_{ISC}, their Φ_P is quite small due to the larger $k_{nr}(T)$ with 10^6 order of magnitude. For compounds **exp3**, **5** and **8**, the Φ_P of them are similar and they are much higher than those of compounds **6** and **7**.

4. Conclusion

In this paper, the vibrationally-resolved phosphorescent spectra and quantum yield of an experimental reported and four novel designed Ir(III) complexes with 2-(2,5,2′,3′,4′,5′,6′-heptafluoro-biphenyl-4-yl)-pyridine (HFYP) as primary ligand are investigated by theoretical calculations both in vacuum and in solvent. Vibrationally-resolved spectra show that there are mainly two strong peaks, which can be ascribed as low-frequency vibrational modes such as the rotation of ligand plane, and benzene ring/pyridine ring in ligand HFYP1 skeleton vibration coupled with C—H in pyridine ring in plane bending vibration. By quantitative calculation of the quantum yields, PLQY of compounds **exp3**, **5** and **8** are relative higher, while those of compounds **6** and **7** are much smaller. This is mainly caused by larger $k_{nr}(T)$, resulting from smaller energy barrier from ^{3}MLCT/LC state to ^{3}MC state of compounds **6** and **7**. The lower barrier may be caused by shorter Ir—N3 bond in the transition state. So in the presence of HFYP primary ligand in Ir(III) complex, pyridin-2-yl-1,2,4-triazolate, 1,2-diazol-5-yl-pyridine are good ancillary ligand, while 2′-oxyphenyl-2-oxazoline is not appropriate to be ancillary ligand. Compared with the vibronic phosphorescence spectra in vacuum, the emission peak position in

solvent shifts to blue within 10 nm and the spectra shape is almost unchanged. By comparison of the quantum yields calculated in vacuum and in solvent, it shows that the quantum yields of compounds **exp3**, **5** and **8** in solvent become smaller.

Acknowledgements

Appendix A. Supplementary data

Supplementary data to this article can be found online at https://doi.org/10.1016/j.saa.2019.03.013.

References

[1] C.L. Ho, H. Li, W.Y. Wong, Red to near-infrared organometallic phosphorescent dyes for OLED applications, J. Organomet. Chem. 751 (2014) 261–285.

[2] B. Jiang, Y. Gu, J.J. Qin, X.W. Ning, S.L. Gong, G.H. Xie, C.L. Yang, Deep-red Iridium(III) complexes cyclometalated by phenanthridine derivatives for highly efficient solution-processed organic light-emitting diodes, J. Mater. Chem. C 4 (2016) 3492–3498.

[3] P. Tao, Y.B. Zhang, J. Wang, L.W. Wei, H.X. Li, X.L. Li, Q. Zhao, X.W. Zhang, S.J. Liu, H. Wang, W. Huang, Highly efficient blue phosphorescent iridium(III) complexes with various ancillary ligands for partially solution-processed organic light-emitting diodes, J. Mater. Chem. C 5 (2017) 9306–9314.

[4] H.T. Mao, C.X. Zang, G.G. Shan, H.Z. Sun, W.F. Xie, Z.M. Su, Achieving high performances of non doped OLEDs using carbazole and diphenylphosphoryl-functionalized Ir(III) complexes as active components, Inorg. Chem. 56 (2017) 9979–9987.

[5] F.L. Zhang, W.L. Li, D.H. Wei, C.Y. Li, C. Pan, X.B. Dong, Z.Y. Li, S.Z. Li, B. Wei, F.Q. Zhang, G.X. Cao, B. Zhai, Synthesis, characterization, photo- and electroluminescent properties of blue cationic iridium complexes with nonconjugated bis(pyrazole-1-yl)methane as the ancillary ligand, Dyes Pigments 134 (2016) 19–26.

[6] W.S. Qu, F.L. Zhang, S.Q. Liu, D.H. Wei, X.B. Dong, B. Yu, W. Lu, C. Zhang, S.Z. Li, Z.Y. Li, B. Wei, B. Zhai, G.X. Cao, Efficient blue electroluminescence of iridium(III) complexes with oxadiazol-substituted amide ancillary ligands, Dyes Pigments 145 (2017) 116–125.

[7] F.L. Zhang, C.F. Si, D.H. Wei, S.S. Wang, D.P. Zhang, S.Z. Li, Z.Y. Li, F.Q. Zhang, B. Wei, G.X. Cao, B. Zhai, Solution-processed organic light-emitting diodes based on yellow-emitting cationic iridium(III) complexes bearing cyclometalated carbene ligands, Dyes Pigments 134 (2016) 465–471.

[8] F.L. Zhang, C.F. Si, X.B. Dong, D.H. Wei, X. Yang, K.P. Guo, B. Wei, Z.Y. Li, C. Zhang, S.Z. Li, B. Zhai, G.X. Cao, Iridium(III) complexes bearing oxadiazol-substituted amide ligands: color tuning and application in highly efficient phosphorescent organic light-emitting diodes, J. Mater. Chem. C 5 (2017) 9146–9156.

[9] H. Guo, J. Zhao, Z. Tian, Y. Wu, B. Liu, F. Dang, X. Yang, G. Zhou, Z. Wu, W.Y. Wong, Homoleptic thiazole-based Ir III phosphorescent complexes for achieving both high EL efficiencies and an optimized trade-off among the key parameters of solution-processed WOLEDs, J. Mater. Chem. C 5 (2017) 208–219.

[10] G. Sarada, B. Sim, C.K. Moon, W. Cho, K.H. Kim, V.G. Sree, E. Park, J.J. Kim, S.H. Jin, Synthesis and characterization of highly efficient blue Ir(III) complexes by tailoring β-diketonate ancillary ligand for highly efficient PhOLED applications, Org. Electron. 39 (2016) 91–5125.

[11] R. Ragni, V. Maiorano, M. Pugliese, A. Maggiore, E. Orselli, F. Babudri, G. Gigli, L. De Cola, G.M. Farinola, A highly fluorinated iridium complex as a blue-green emitting component for white electroluminescence, Synth. Met. 227 (2017) 148–155.

[12] F. Babudri, G.M. Farinola, F. Naso, R. Ragni, Fluorinated organic materials for electronic and optoelectronic applications: the role of the fluorine atom, Chem. Commun. 10 (2007) 1003–1022.

[13] B. Milián-Medina, S. Varghese, R. Ragni, H. Boerner, E. Ortí, G.M. Farinola, J. Gierschner, Excited-state switching by per-fluorination of para-oligophenylenes, J. Chem. Phys. 235 (2011) 214509–1-6.

[14] C. Martinelli, U. Giovanella, A. Cardone, S. Destri, G.M. Farinola, A white emitting poly(phenylenevinylene), Polymer 55 (2014) 5125–5131.

[15] P. Tao, W.L. Li, J. Zhang, S. Guo, Q. Zhao, H. Wang, B. Wei, S.J. Liu, X.H. Zhou, Q. Yu, B.S. Xu, W. Huang, Facile synthesis of highly efficient lepidine-based phosphorescent iridium(III) complexes for yellow and white organic light emitting diodes, Adv. Funct. Mater. 26 (2016) 881–894.

[16] B. Minaev, V. Minaeva, H. Ågren, Theoretical study of the cyclometalated iridium(III) complexes used as chromophores for organic light-emitting diodes, J. Phys. Chem. A 113 (2009) 726–735.

[17] X. Li, B. Minaev, H. Ågren, H. Tian, Theoretical study of phosphorescence of iridium complexes with fluorine-substituted phenylpyridine ligands, Eur. J. Inorg. Chem. 2011 (2011) 2517–2524.

[18] L. Tian, Y. Luo, L. Zhang, M. Li, R. He, W. Shen, Theoretical insight into the role of triarylboron substituents in tetradentate dianionic bis(N-heterocyclic carbene) Platinum(II) chelates-improving the performance of blue light emission, Eur. J. Inorg. Chem. 2015 (2015) 1902–1911.

[19] C.Y. Shang, J. Xu, Y.Q. Du, J. Zhao, Investigation on the electronic structures and photophysical properties of a series of cyclometalated iridium(III) complexes based on DFT/TDDFT calculations, J. Lumin. 175 (2016) 217–224.

[20] G.S.M. Tong, P.K. Chow, W.P. To, W.M. Kwok, C.M. Che, A theoretical investigation into the luminescent properties of d8-transition-metal complexes with tetradentate schiff base ligands, Chem. Eur. J. 20 (2014) 1–12.

[21] D. Escudero, Quantitative prediction of photoluminescence quantum yields of phosphors from first principles, Chem. Sci. 7 (2016) 1262–1267.

[22] Q. Zhang, X.L. Wang, X. Wang, L. Wang, J.L. Zhang, Computational studies of electronic structures and photophysical properties of luminescent iridium(III) complexes based on amidinate/bis(pyridylphenyl) ligands, Org. Electron. 33 (2016) 281–289.

[23] Q. Zhang, X. Wang, Y. Zhang, L. Wang, J.F. Li, J.L. Zhang, Insight into the phosphorescent process of cyclometalated Ir(III) complexes: combination of the substituents on primary and ancillary ligands controls the emission rule and quantum yield, J. Phys. Chem. C 120 (2016) 27523–27532.

[24] X.L. Wang, Y. Ma, S.Y. Feng, L. Wang, J.F. Li, J.L. Zhang, Exploring the influence of different ancillary ligands of heteroleptic Ir(III) complexes on the phosphorescent properties: emissive rule and photodeactivation dynamics, Org. Electron. 41 (2017) 251–258.

[25] X.L. Wang, Y.Y. Li, L. Wang, J.L. Zhang, Theoretical studies on cyclometalated platinum(II) complexes based on isoquinolinyl azolate: ππ-stacking interaction and photophysical properties, Org. Electron. 35 (2016) 208–215.

[26] X.L. Wang, H.Q. Yang, Y.P. Wen, L. Wang, J.F. Li, J.L. Zhang, Comprehension of the effect of a hydroxyl group in ancillary ligand on phosphorescent property for heteroleptic Ir(III) complexes: a computational study using quantitative prediction, Inorg. Chem. 56 (2017) 8986–8995.

[27] X.L. Wang, C. Chen, Y.Y. Li, P. Ning, W.P. Wu, L. Wang, To design high efficient red-emitting iridium complexes by variation of ancillary ligand: emissive rule and quantum yield, Org. Electron. 49 (2017) 360–367.

[28] J.Y. Guo, X. Pan, X.L. Wang, W.P. Wu, J.L. Zhang, Theoretical study on the vibrationally resolved spectra and quantum yield of blue phosphorescent iridium(III) complexes with 2-(4-fluoro-3-(trifluoromethyl)-phenyl)pyridine as the cyclometalated ligand, Org. Electron. 61 (2018) 125–133.

[29] J.Q. Li, L. Wang, X. Wang, J.L. Zhang, X.F. Cui, Y.W. Li, B.K. Han, Theoretical perspective of FIrpic derivatives: relationship between structures and photophysical properties, Spectrochim. Acta A 171 (2017) 425–431.

[30] Q. Peng, Q. Shi, Y. Niu, Y. Yi, S. Sun, W. Li, Z. Shuai, Understanding the effciency drooping of the deep blue organometallic phosphors: a computational study of radiative and non-radiative decay rates for triplets, J. Mater. Chem. C 4 (2016) 6829–6838.

[31] X. Zhang, D. Jacquemin, Q. Peng, Z. Shuai, D. Escudero, General approach to compute phosphorescent OLED efficiency, J. Phys. Chem. C 122 (2018) 6340–6347.

[32] W.P. Wu, Z.X. Cao, Y. Zhao, Theoretical studies on absorption, emission, and resonance Raman spectra of coumarin 343 isomers, J. Chem. Phys. 136 (2012), 114305. .

[33] K. Chao, K. Shao, T. Peng, D. Zhu, Y. Wang, Y. Liu, Z. Su, M.R. Bryce, New oxazoline-and thiazoline-containing heteroleptic iridium(III) complexes for highly-efficient phosphorescent organic light-emitting devices (PhOLEDs): colour tuning by varying the electroluminescence bandwidth, J. Mater. Chem. C 1 (2013) 6800–6806.

[34] H. Benjamin, M.A. Fox, A.S. Batsanov, H.A. Al-Attar, C. Li, Z. Ren, A.P. Monkman, M.R. Bryce, Pyridylpyrazole N^N ligands combined with sulfonyl-functionalised cyclometalating ligands for blue-emitting iridium(III) complexes and solution-processable PhOLEDs, Dalton Trans. 46 (2017) 10996–11007.

[35] A.D. Becke, Density-functional thermochemistry. III. The role of exact exchange, J. Chem. Phys. 98 (1993) 5648–5652.

[36] C. Lee, W.T. Yang, R.G. Parr, Development of the Colle-Salvetti correlation-energy formula into a functional of the electron density, Phys. Rev. B 37 (1988) 785–789.

[37] P.J. Hay, W.R. Wadt, Ab initio effective core potentials for molecular calculations. Potentials for K to Au including the outermost core orbitals, J. Chem. Phys. 82 (1985) 299–310.

[38] P.J. Hay, W.R. Wadt, Ab initio effective core potentials for molecular calculations. Potentials for the transition metal atoms Sc to Hg, J. Chem. Phys. 82 (1985) 270–283.

[39] P.C. Hariharan, J.A. Pople, Accuracy of AH n equilibrium geometries by single determinant molecular orbital theory, Mol. Phys. 27 (1974) 209–214.

[40] J.N. Harvey, M. Aschi, Spin-forbidden dehydrogenation of methoxy cation: a statistical view, Phys. Chem. Chem. Phys. 1 (1999) 5555–5563.

[41] J.N. Harvey, M. Aschi, H. Schwarz, W. Koch, The singlet and triplet states of phenylcation. A hybrid approach for locating minimum energy crossing points between non-interacting potential energy surfaces, Theor. Chem. Accounts 99 (1998) 95–99.

[42] B.I. Lundqvist Gunnarsson, Exchange and correlation in atoms, molecules, and solids by the spin-density-functional formalism, Phys. Rev. B 13 (1976) 4274–4298.

[43] T. Ziegler, Approximate density functional theory as a practical tool in molecular energetics and dynamics, Chem. Rev. 91 (1991) 651–667.

[44] Dalton, a molecular electronic structure program, Release Dalton 2011 (2011), see http://daltonprogram.org.

[45] M. Cossi, V. Barone, B. Mennucci, J. Tomasi, Ab initio study of ionic solutions by a polarizable continuum dielectric model, Chem. Phys. Lett. 286 (1998) 253–260.

[46] M.J. Frisch, G.W. Trucks, H.B. Schlegel, G.E. Scuseria, M.A. Robb, J.R. Cheeseman, G. Scalmani, V. Barone, B. Mennucci, G.A. Petersson, H. Nakatsuji, M. Caricato, X. Li, H.P. Hratchian, A.F. Izmaylov, J. Bloino, G. Zheng, J.L. Sonnenberg, M. Hada, M.

Ehara, K. Toyota, R. Fukuda, J. Hasegawa, M. Ishida, T. Nakajima, Y. Honda, O. Kitao, H. Nakai, T. Vreven, J.A. Montgomery, J.E. Peralta, F. Ogliaro, M. Bearpark, J.J. Heyd, E. Brothers, K.N. Kudin, V.N. Staroverov, R.K. Obayashi, J. Normand, K. Raghavachari, A. Rendell, J.C. Burant, S.S. Iyengar, J. Tomasi, M. Cossi, N. Rega, J.M. Millam, M. Klene, J.E. Knox, J.B. Cross, V. Bakken, C. Adamo, J. Jaramillo, R. Gomperts, R.E. Stratmann, O. Yazyev, A.J. Austin, R. Cammi, C. Pomelli, J.W. Ochterski, R.L. Martin, K. Morokuma, V.G. Zakrzewski, G.A. Voth, P. Salvador, J.J. Dannenberg, S. Dapprich, A.D. Daniels, O. Farkas, J.B. Foresman, J.V. Ortiz, J. Cioslowski, D.J. Fox, Gaussian 09, Revision B.01, Gaussian, Inc., Wallingford, CT, 2010.

[47] Z.G. Shuai, Q. Peng, Excited states structure and processes: understanding organic light-emitting diodes at the molecular level, Phys. Rep. 537 (2014) 123–156.

[48] Z.G. Shuai, Q. Peng, Y.L. Niu, H. Geng, MOMAP, a free and open-source molecular materials property prediction package, Revision 0.2.004; Shuai group: Beijing, China, 2014, http://www.shuaigroup.net/.

[49] Q. Peng, Y. Yi, Z. Shuai, J. Shao, Excited state radiation less decay process with Duschinsky rotation effect: formalism and implementation, J. Chem. Phys. 126 (2007) 114302–114308.

[50] Y. Niu, Q. Peng, C. Deng, X. Gao, Z. Shuai, Theory of excited state decaysand optical spectra: application to polyatomic molecules, J. Phys. Chem. A 114 (2010) 7817–7831.

[51] K. Dedeian, J.M. Shi, N. Shepherd, E. Forsythe, D.C. Morton, Photophysical and electrochemical properties of heteroleptic tris-cyclometalated Iridium(III) complexes, Inorg. Chem. 44 (2005) 4445–4447.